International Symposium
On Turbulence and Shear Flow
Phenomena (TSFP-9)
June 30 - July 3, 2015 *Melbourne, Australia*

DIRECT SIMULATION OF FLOW OVER A WALL-MOUNTED HUMP

Susheel Sekhar
NASA Advanced Supercomputing Division
NASA Ames Research Center
Moffett Field, CA 94035
susheel.sekhar@nasa.gov

Nagi N. Mansour
NASA Advanced Supercomputing Division
NASA Ames Research Center
Moffett Field, CA 94035
nagi.n.mansour@nasa.gov

ABSTRACT

Simulating separated flows at high Reynolds numbers using Reynolds Averaged Navier-Stokes (RANS) modeled equations remains a challenge in aeronautics. The main hindrance to progress stems from the lack of extended detailed data pertinent to the root cause of failure of RANS models, as well as the little progress in RANS modeling innovations in the past several decades. The goal of the current effort is to generate data for separated flow at a Reynolds numbers where conventional models are challenged. We use Direct Numerical Simulations to model turbulent flow over the wall-mounted hump configuration to investigate the physics of flow separation and boundary layer recovery, as well as provide data relevant to the modeling community. A chord-based Reynolds number of Re_c = 47,500 is considered with a turbulent inflow profile of Re_θ = 1,400 (θ/c = 3%). We use FDL3DI, a code that solves the compressible Navier-Stokes equations using high-order compact-difference scheme and filter, with the standard recycling/rescaling method of generating turbulent boundary layers as inflow to the computational domain. Two different configurations of the upper-wall are analyzed for two sets of boundary conditions (slip and no-slip). The results are compared with the available higher Re_c (= 936,000, Re_θ = 7,200, θ/c = 0.77%) experiment for major flow features. The simulated lower Re_c allows for DNS-like mesh resolutions, and adequately wide spans. The results from these simulations show earlier separation and delayed reattachment compared to Re_c = 936,000, and significantly higher skin friction in the forebody of the hump. We also find that the upper-wall shape and boundary condition influence pressure distribution over the hump, whereas skin friction is only influenced by the boundary condition.

INTRODUCTION

Accurate prediction of turbulent boundary layer flows at high Reynolds numbers continues to be a significant problem in computational fluid dynamics (CFD). When such boundary layers separate, simulations become all the more challenging as our understanding of the underlying physics is still incomplete. Most turbulent flows in engineering applications are simulated using various models that represent understood physics. However, there is still no universal model that can be used to compute every turbulent flow scenario. This paper is aimed at understanding the physical underpinnings of observed flow phenomena, with the aim of providing data to improve turbulence models.

The Langley Research Center Workshop on CFD Validation of Synthetic Jets and Turbulent Separation Control (Rumsey *et al.* (2006); Rumsey (2007*a*); Rumsey (2008)) was organized in 2004 with the aim to bring together practitioners to assess current capabilities. The workshop provided cases that challenge various aspects of the failure of the state of the art models. Case 3 at the workshop is turbulent flow over a wall-mounted hump configuration. This setup consisted of a Glauert-Goldschmied-type airfoil mounted between two glass end-plates, and was based on earlier experiments of Seifert & Pack (2002), who had studied flows over a similar configuration at higher Reynolds numbers ($\mathrm{Re}_c = 2.4 - 2.6 \times 10^6$, based on chord-length). The baseline experiment at the workshop by Greenblatt *et al.* (2006) had an Re_c = 936,000, with a turbulent inflow Re_θ = 7,200 at M_∞ = 0.1. Both leading and trailing edges were faired smoothly with a wind tunnel splitter plate, whereas the experiments of Seifert & Pack installed the airfoil on the wind tunnel floor. This baseline case without flow-control showed that flow separates near 65% of the chord, and reattaches downstream past the hump (at x/c = 1.1 $\pm$ 0.003 from the leading edge). In addition to C_p and C_f distributions, 2D/stereo PIV data of velocity profiles and turbulence quantities along the tunnel center plane were documented.

At the 2004 and many subsequent workshops, this case has been analyzed extensively. Numerous RANS studies were conducted, and all failed to reproduce many characteristics of this flow. RANS models were inconsistent in predicting the size of the separation bubble because eddy-viscosity and Reynolds stresses were under-predicted within the separation region. Rumsey (2007*b*) showed that doubling eddy-viscosity in a region near the separation bubble did indeed result in earlier reattachment, and a bubble

size more comparable with experiment. Some LES and hybrid RANS/LES methods made much better predictions of the flow features. A summary of the successes and shortcomings of these methods was presented in an earlier paper by the authors (Sekhar *et al.* (2015)).

Postl & Fasel (2006) conducted the only known simulation with DNS-like resolution for this case (using the incompressible vorticity-velocity form of the Navier-Stokes equations). Their mesh had $\Delta x^+ = 27 - 92$, $\Delta y^+ = 1.2$, $\Delta z^+ = 17$, and a span of $0.142c$. In addition to being under-resolved, a thinner laminar inflow profile with Re_θ = 4,000 at x/c = -0.5 was used (this is equivalent to Re_θ = 2,400 at x/c = -2.14, $\theta/c = 0.26\%$). The boundary layer was tripped near the inflow using a time-harmonic forcing term. With that setup, the separation point and mean velocity profile before separation matched well with experiment. But the size of the separation bubble and reattachment point were both over-predicted by about 20%. This was attributed to the relative coarseness of the mesh, which failed to resolve the smallest scales adequately. Further, lack of information about freestream turbulence intensity added to these discrepancies, particularly in the range of frequencies where the separated shear layer is hydrodynamically unstable.

Seifert & Pack (2002) noted that, for the given fully turbulent inflow conditions, the characteristics of separation and the bubble length were largely insensitive to the inflow Re_θ and Re_c. This was especially true since laminar to turbulent transition was eliminated in the domain. But the ratio of the thickness of the incoming boundary layer to the hump height (δ/h) played a significant part. In other words, matching experimental θ/c (momentum thickness to chord ratio) is critical in replicating the conditions for similar flow separation. Postl & Fasel (2006) also attributed differences between their DNS and experiment to the narrow span width.

Given the computational costs of setting up DNS at the experimental conditions (estimated to be upwards of 6 billion grid points with the current setup), a test case of lower Re_θ:Re_c flow over the wall-mounted hump is considered in this paper. In compromising on the θ/c ratio, we are able to realize a mesh resolution finer than any prior DNS, and a wide-enough span to enable the capture of uncorrelated streaks. This was conducted as the first step towards setting up simulations at experimental θ/c, in addition to lending an extra data-point to the literature, considering the lack of high quality DNS for this configuration. Comparisons of surface pressure and skin friction, as well as mean velocity and Reynolds stress profiles, were made with the available experimental data at the lower θ/c.

NUMERICAL METHOD

The finite-difference code, a variant of AFRL's FDL3DI (Gaitonde & Visbal (1998); Morgan *et al.* (2002)), used in this study solves the compressible Navier-Stokes equations for an ideal gas. The sixth-order compact-difference scheme of Lele (1992) is used to solve the governing equations in transformed curvilinear coordinates (Rizzetta *et al.* (1999); Visbal *et al.* (2003)). Fourth-order explicit Runge-Kutta (RK-4) is used for time integration. During each time step, an eighth-order low-pass spatial filtering scheme is applied to the conservative variables to ensure stability, along with second- and fourth-order near-boundary formulations of Gaitonde & Visbal (2000). A filtering optimization parameter of $\alpha_f = 0.495$ is set. This results in less dissipation compared to the ILES of the same configuration by Morgan *et al.* (2005) ($\alpha_f = 0.4$) and Franck & Colonius (2008) ($\alpha_f = 0.45$). Other than the low-pass filter, no additional sub-grid scale model is used. Spatial resolution demands are dictated by choice of numerical schemes, and sixth-order Padé requires 60% finer meshes than those required for Fourier spectral methods. Thus, even with DNS-like resolution, this effort is considered under-resolved. To ensure stability and accuracy of time integration, a Courant-Friedrichs-Lewy (CFL) number in the vicinity of 0.4, based on the acoustic speeds, is used in the RK-4 scheme.

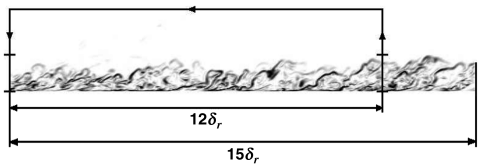

Figure 1. Recycling-rescaling methodology schematic (Morgan (2012))

For generating a turbulent inflow, the standard recycling/rescaling method of Lund *et al.* (1998) is used in the code. Urbin & Knight (2001) extended this method to compressible flows for solving a Mach 3 turbulent boundary layer. This was implemented as a part of the effort to study the interaction of an oblique shock wave and a turbulent boundary layer by Morgan *et al.* (2011) The approach extracts the instantaneous velocity profile from a plane downstream of the inflow, then rescales and reintroduces it as the inflow. The schematic of the procedure is given in Fig. 1. It has been shown to produce a realistic turbulent boundary layer, yielding statistics that are in good agreement with experiment and DNS. To further prevent contamination of the solution with spurious spatio-temporal correlations generated by this reintroduction procedure, a non-constant reflection of the recycled turbulence plane is applied at randomly distributed time intervals. This method, termed recycling/rescaling with dynamic reflection (RR+DR), has been used to solve subsonic flows here. It eliminates the need for freestream turbulence intensity data, the lack of which further handicapped Postl & Fasel's DNS.

TURBULENT INFLOW

The turbulent inflow profile with $\mathrm{Re}_\theta = 1,400$ was generated as a simultaneous auxiliary simulation. A domain of length $15\delta_\mathrm{R}$, height $3\delta_\mathrm{R}$ and span $1\delta_\mathrm{R}$ was used, where δ_R is the desired boundary layer thickness at the velocity capture-plane. The height of the domain was chosen based on the validation study of Lund *et al.* (1998) for the same Re_θ. The spanwise width was identified in a parametric study by the authors (Sekhar & Mansour (2015)) that investigated the minimum width required for turbulent boundary layers to match reference DNS. The inflow capture-plane was located $12\delta_\mathrm{R}$ downstream of the inlet, and was also the location of the target Re_θ (Fig. 4). This mesh consisted of $500 \times 100 \times 105$ points, and was uniformly spaced along streamwise and spanwise directions. A hyperbolic tangent stretching was used in the wall-normal direction. The mesh resolution at the wall was a DNS-like $\Delta x^+ = 19.4$, $\Delta y^+ = 0.65$, $\Delta z^+ = 6$. The inflow profile was validated by comparing the mean velocity profile with the spectral DNS

of Spalart (1988) (Fig. 2).

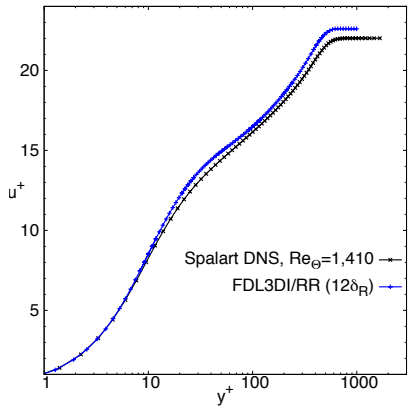

Figure 2. Mean u in wall units at x/c = -2.14, compared with DNS of Spalart (1988)

There is very good agreement through the viscous sublayer and the log layer. The slightly higher freestream velocity at the edge of the boundary layer is attributed to the upper-wall boundary condition. Whereas the reference DNS corresponds to a zero pressure-gradient flat plate boundary layer, the current upper-wall in the inflow domain is set to a symmetry boundary. This results in a slight acceleration of the freestream.

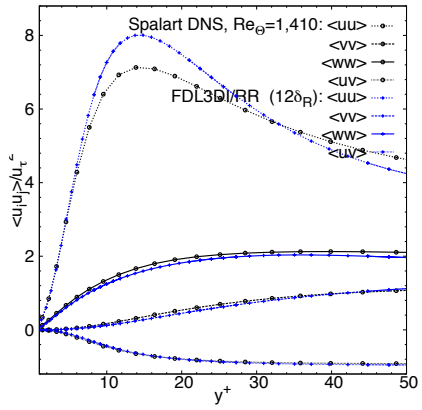

Figure 3. Re stresses in the viscous near-wall region, normalized by u_τ, at x/c = -2.14, compared with DNS of Spalart (1988)

Figure 3 compares the Reynolds stresses in the viscous near-wall region. Differences in $<uu>/u_\tau^2$ are evident within the buffer layer, whilst the rest of the stresses agrees with the reference. This over-prediction within the buffer layer, also evident in the mean velocity profile, has been shown to be due to differences in the upper-wall boundary condition and compressibility effects (Spectral DNS $M_\infty = 0.1$ vs current DNS $M_\infty = 0.3$).

WALL-MOUNTED HUMP

Dimensions of the hump domain were defined in the CFDVAL2004 workshop. The inflow plane was located 2.14 chord-lengths (c) upstream of the leading edge of the hump, and the exit plane was 4.0c downstream. The height from the splitter-plate to the upper wall was 0.90905c. Therefore, Re_c was computed based on the constraints set by the dimensions of the inflow and hump domains, i.e. $3\delta_R = 0.90905c$ (Fig. 4). The theoretical δ_R for this inflow, based on Prandtl's one-seventh power law, was computed to be 0.002061 m, resulting in $c = 0.0068$ m. The experimental c was 0.42 m. With $M_\infty = 0.3$, these simulations were set for a $Re_c \approx 47,500$, which is one-twentieth of the experimental Re_c (= 936,000). The θ/c ratio was, therefore, computed to be 3%, compared to the experimental θ/c of 0.77%, and 0.26% in Postl & Fasel's setup. Morgan *et al.* (2005) conducted a coarser ILES of the same configuration with Re_c = 200,000 and θ/c = 3.6%. Also, Franck & Colonius (2008) showed that this configuration is insensitive to differences in M_∞ from 0.1 to 0.3.

Two meshes (Fig. 5) that differed in the shape of the upper-wall were considered. During the CFDLVAL2004 workshop, the top-wall shape was modified to account for side-wall blockage effects, which improved the pressure distribution over the hump. At this higher θ/c, both upper-wall profiles were simulated to document differences at the current flow conditions. "struct1" corresponds to the flat upper-wall, and "struct4" is the contoured shape. Each mesh consisted of $827 \times 100 \times 105$ points, with a similar DNS-like resolution at the wall ($\Delta x^+ \leq 19.4$, $\Delta y^+ = 0.65$, $\Delta z^+ = 6$). Postl & Fasel (2006) in their under-resolved DNS used a mesh with $\Delta x^+ = 27 - 92$, $\Delta y^+ = 1.2$, $\Delta z^+ = 17$, on a domain of span 0.142c. The current setup has a span of 0.3c. This setup, therefore, address both drawbacks cited in their paper, despite being for a higher θ/c.

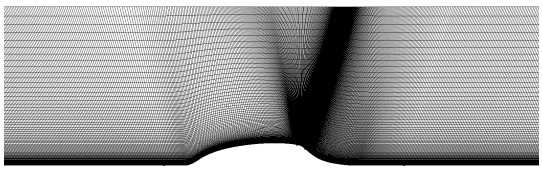

(a) struct1: flat upper-wall

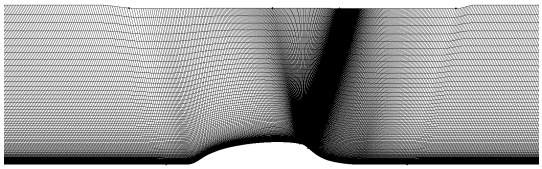

(b) struct4: contoured upper-wall

Figure 5. Meshes used: $827 \times 100 \times 105$ points

In addition to the two different shapes for the upper-wall, slip and no-slip boundary conditions here were simulated. For the remaining boundaries, a P_∞ outflow was set at the outlet, a no-slip, adiabatic wall was used for the bottom wall, and along the span, periodic boundaries were set.

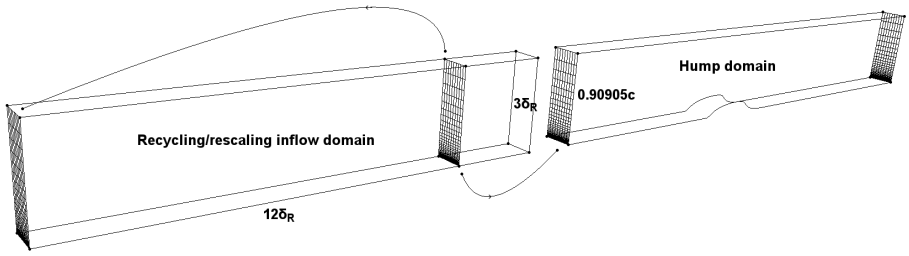

Figure 4. Perspective view of the schematic of the computational setup

RESULTS

Non-dimensionlized mean velocity contours at the spanwise mid-plane are shown in Fig. 6. Figure 6 (a) shows experimental 2D PIV results for the Re_c = 936,000 case, and Figs. 6 (b)-(e) represent the simulation results for Re_c = 47,500 using meshes "struct1" and "struct4," with no-slip and slip upper-walls, respectively, averaged over 10 flow-through times (FTTs). The first observation that stands out is the longer separation region at higher θ/c (3%). Both upper-wall shapes predict the reattachment point downstream of that for experiment with θ/c = 0.77%. In addition, the point of separation is further upstream. There is little difference between the two upper-wall shapes, and a further delayed reattachment is evident with the slip-wall boundary condition. Both earlier separation and delayed reattachment at θ/c = 3% conform with those seen in the ILES of Morgan *et al.* (2005), whose θ/c was a comparable 3.6%.

For a quantitative estimate of the flow features, surface pressure and skin friction along the wall were compared. C_p values for the simulations presented have been appropriately shifted to match the experimental freestream conditions. Simulations with both upper-wall shapes and boundary conditions were analyzed. In Fig. 7 (a), surface pressure computed over the fore-body of the hump are higher than the Re_c = 936,000 experiment, but are lower within the separation bubble. Higher pressure over the fore-body was also observed in the ILES of Morgan et al., but C_p within the bubble is reversed: whereas their ILES showed higher pressure within the separation bubble compared to experiment, all of the current simulations show significantly lower C_p here (30-100% lower). When comparing upper-wall shapes, the modified shape does produce a lower C_p before separation that is comparable to experiment. When the upper surface is set to a slip-wall, surface pressures for both shapes are virtually identical; the channel-like acceleration of the freestream that was observed with the no-slip wall is absent here, resulting in a lower pressure definition over the hump and an insensitivity to the shape of the upper-wall.

Figure 7 (b) shows the comparison of skin friction along the surface. Here too, observations similar to Morgan et al. are evident: a higher θ/c results in a significantly higher C_f in the fore-body of the hump. Whereas their peak C_f was 0.01, the current simulations have them between 0.013-0.015, almost twice that of the experiment. With no-slip upper-boundaries, differences in magnitude are evident along the fore-body of the hump; the modified shape causes slightly higher velocities, and therefore skin friction. Skin friction values within the separation bubble and downstream of reattachment are identical. When the upper-boundary is set to a slip wall, both upper-wall shapes result in identical skin friction profiles over the entire surface. Compared to the no-slip condition, the magnitudes are less on the fore-body, but the point of separation is the same ($\approx$ 55% chord). Reattachment with this boundary condition is delayed even further compared to the no-slip upper wall. For the slip-walls, this point is approximately at x/c = 1.3, whereas for the no-slip walls, reattachment occurs at x/c = 1.25. The experimental reattachment point for θ/c = 0.77% is at

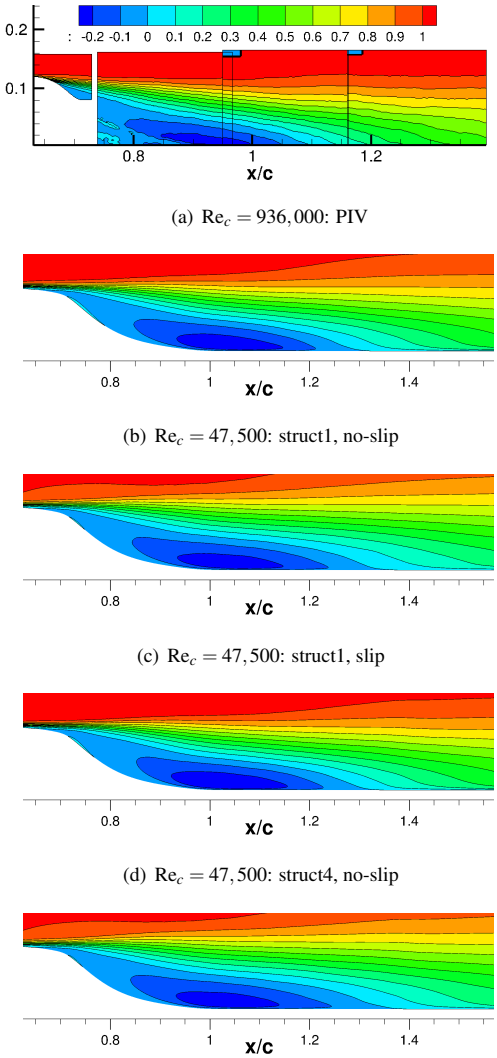

(a) $\mathrm{Re}_c = 936{,}000$: PIV

(b) $\mathrm{Re}_c = 47{,}500$: struct1, no-slip

(c) $\mathrm{Re}_c = 47{,}500$: struct1, slip

(d) $\mathrm{Re}_c = 47{,}500$: struct4, no-slip

(e) $\mathrm{Re}_c = 47{,}500$: struct4, slip

Figure 6. Contours of U/U_∞, averaged over 10FTTs

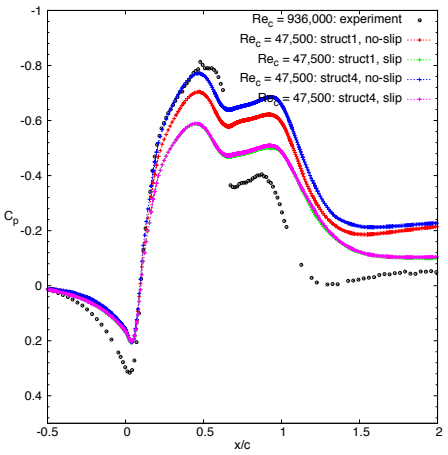

(a) C_p

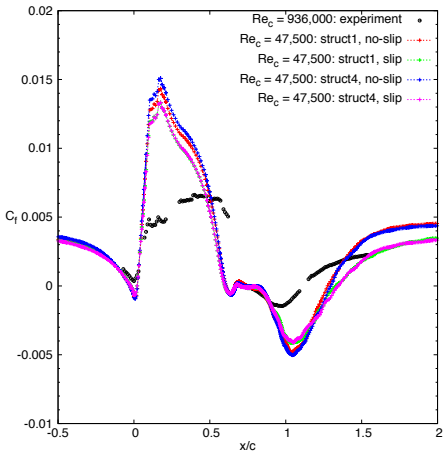

(b) C_f

Figure 7. Pressure and skin friction variation

$x/c \approx 1.1$. The simulations also show a secondary separation bubble between 50% and 60% chord, which is absent in the experiment.

To analyze boundary layer recovery, mean streamwise and wall normal components of flow velocity at different locations downstream of separation are compared in Fig. 8. Considering differences in θ/c between the simulations and experiment, to make a better estimate of turbulent boundary layer recovery, the axial location of reattachment for the experiment was shifted downstream to coincide with the simulations. Results from the cases with no-slip upper-walls are compared. The overall trend of recovery shows very good agreement for both θ/c inflow profiles. The experiment with the relatively thinner profile is slightly offset downstream, and this is attributed to differences in the Reynolds number. But the shapes of both U and V match very well. Marginal differences between the simulations with different upper-wall shapes are evident only in the freestream.

Comparisons of the mean Reynolds stress components $<uu>$, $<vv>$ and $<uv>$ at the same x/c locations are presented in Fig. 9. A similar strategy was followed in shifting the separation point for the experiment, and the overall trends compare well here as well.

SUMMARY

Simulations of flow over the wall-mounted hump configuration have been conducted with a thicker inflow profile compared to experiment. By compromising on the θ/c ratio (3% vs 0.77%) DNS-like mesh resolutions, and an adequate span widths can be achieved. Qualitative comparisons with experimental data show an earlier separation for the higher θ/c simulations and delayed reattachment. Overall trends of surface pressure and skin friction agree, but their magnitudes are vastly different. The simulations show significantly higher surface pressures and skin friction in the fore-body of the hump and lower pressures within the separation bubble. When analyzing recovery, the trends in terms of mean velocity profiles and the Reynolds stresses downstream of reattachment are nearly identical to the experiment, displaying patterns that are independent of the Reynolds number.

Meshes with different upper-wall shapes were compared, and the velocity profiles and Reynolds stresses predicted using each were identical, as was the skin friction. There are differences, though, in the surface pressure over the fore-body of the hump, as well as within the separation bubble. But, this clearly has very little impact on the characteristics of separation, in terms of the point of separation, reattachment, or recovery. When a slip-wall is set at the upper boundary, the magnitudes of the surface pressures using both upper-wall shapes are identical to each other, and are smaller than with the no-slip upper boundary. The point of separation continues to be the same, but reattachment is delayed by about 10%.

ACKNOWLEDGEMENTS

This research is supported by an appointment to the NASA Postdoctoral Program at Ames Research Center, administered by Oak Ridge Associated Universities through a contract with NASA. The authors are grateful for the support of NASA's Aeronautics Research Mission Directorate (ARMD) through the Transformative Aeronautics Concept (TAC) Program's Transformational Tools & Technologies (T3) Project: Revolutionary Tools & Methods (RTM).

REFERENCES

Franck, J.A. & Colonius, T. 2008 Large-eddy simulations of separation control for compressible flow over a wall-mounted hump. In *46th AIAA Aerospace Sciences Meeting and Exhibit*. AIAA 2008-0555.

Gaitonde, D.V. & Visbal, M.R. 1998 High-order schemes for Navier-Stokes equations: Algorithm and implementation into FDL3DI. AFRL-VA-WP TR-1998-3060.

Gaitonde, D.V. & Visbal, M.R. 2000 Padé-type higher-order boundary filters for the Navier-Stokes equations. *AIAA Journal* **38** (11), 2103–2112.

Greenblatt, D., Paschal, K.B., Yao, C.-S., Harris, J., Schaeffler, N.W. & Washburn, A.E. 2006 Experimental investigation of separation control part 1: Baseline and steady suction. *AIAA Journal* **44** (12), 2820–2830.

Lele, S.K. 1992 Compact finite difference schemes with spectral-like resolution. *Journal of Computational Physics* **103**, 16–42.

Lund, T.S., Wu, X. & Squires, K.D. 1998 Generation of turbulent inflow data for spatially-developing boundary layer simulations. *Journal of Computational Physics* **140**, 233–258.

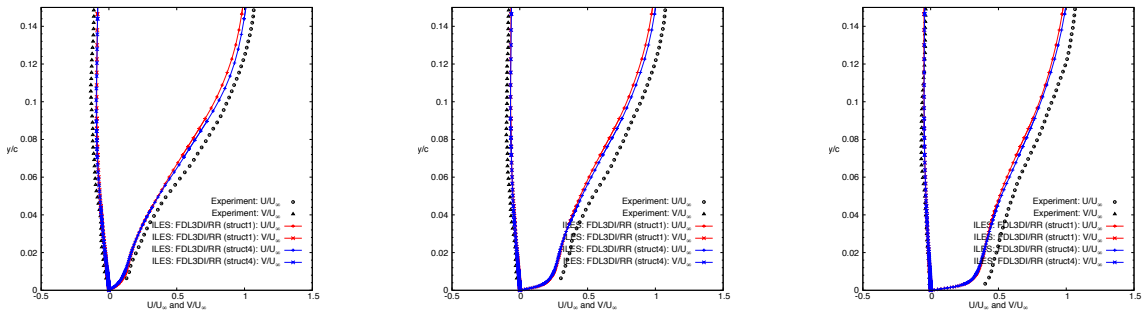

(a) x/c=1.3 (b) x/c=1.4 (c) x/c=1.5

Figure 8. Velocity profiles (U/U_∞ and V/U_∞) at streamwise locations; x/c for experiment is shifted to match simulations

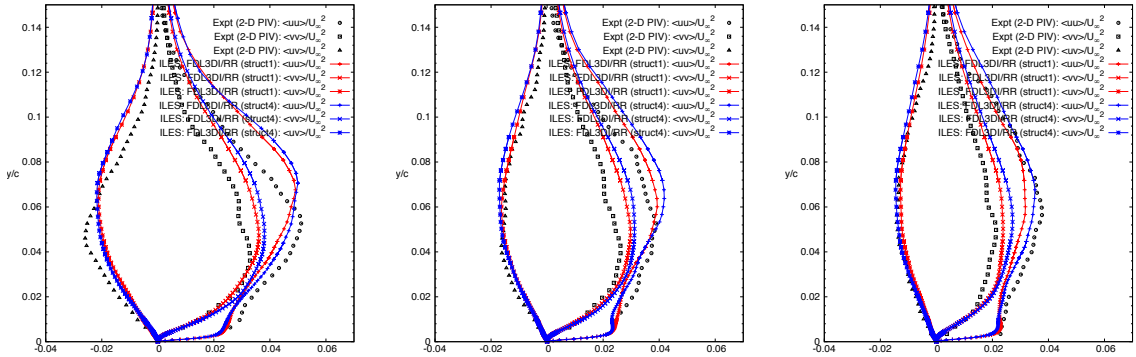

(a) x/c=1.3 (b) x/c=1.4 (c) x/c=1.5

Figure 9. Mean Re stress profiles ($<uu>/U_\infty^2$, $<vv>/U_\infty^2$ and $<uv>/U_\infty^2$) at streamwise locations

Morgan, B.E. 2012 Large-eddy simulation of shock/turbulence interactions in hypersonic vehicle isolator systems. PhD thesis, Stanford University, Stanford, CA.

Morgan, B.E., Larsson, J., Kawai, S. & Lele, S.K. 2011 Improving low-frequency characteristics of recycling/rescaling inflow turbulence generation. *AIAA Journal* **49** (3), 582–597.

Morgan, P.E., Rizzetta, D.P. & Visbal, M.R. 2005 Large-eddy simulation of flow over a wall-mounted hump. In *43rd AIAA Aerospace Sciences Meeting and Exhibit*. AIAA 2005-0484.

Morgan, P.E., Visbal, M.R. & Rizzetta, D.P. 2002 A parallel high-order flow solver for large-eddy and direct numerical simulation. In *32nd AIAA Fluids Dynamics Conference and Exhibit*. AIAA 2002-3123.

Postl, D. & Fasel, H.F. 2006 Direct numerical simulation of turbulent flow separation from a wall-mounted hump. *AIAA Journal* **44** (2), 263–272.

Rizzetta, D.P., Visbal, M.R. & Blaisdell, G.A. 1999 Application of a high-order compact difference scheme to large-eddy and direct numerical simulation. In *30th AIAA Fluid Dynamics Conference*. AIAA 1999-3714.

Rumsey, C.L. 2007*a* Proceedings of the 2004 workshop on CFD validation of synthetic jets and turbulent separation control. *Tech. Rep.* NASA/CP-2007-214874.

Rumsey, C.L. 2007*b* Reynolds-averaged Navier-Stokes analysis of zero efflux flow control over a hump model. *Journal of Aircraft* **44** (2), 444–452.

Rumsey, C.L. 2008 Successes and challenges for flow control simulations (invited). In *4th AIAA Flow Control Conference*. AIAA 2008-4311.

Rumsey, C. L., Gatski, T. B., III, W. L. Sellers, Vatsa, V. N. & Viken, S. A. 2006 Summary of the 2004 computational fluid dynamics validation workshop on synethetic jets. *AIAA Journal* **44** (2), 194–207.

Seifert, A. & Pack, L.G. 2002 Active flow separation control on wall-mounted hump at high Reynolds numbers. *AIAA Journal* **40** (7), 1363–1372.

Sekhar, S. & Mansour, N.N. 2015 Implicit large-eddy simulations of zero-pressure gradient, turbulent boundary layer. In *53rd AIAA Aerospace Sciences Meeting*. AIAA 2015-1987.

Sekhar, S., Mansour, N.N. & Caubilla, D.H. 2015 Implicit LES of turbulent, separated flow: wall-mounted hump configuration. In *53rd AIAA Aerospace Sciences Meeting*. AIAA 2015-1966.

Spalart, P.R. 1988 Direct simulation of a turbulent boundary layer up to $\mathrm{Re}_\theta = 1410$. *Journal of Fluid Mechanics* **187**, 61–98.

Urbin, G. & Knight, D. 2001 Large-eddy simulation of a supersonic boundary layer using an unstructured grid. *AIAA Journal* **39** (7), 1288–1295.

Visbal, M.R., Morgan, P.E. & Rizzetta, D.P. 2003 An implicit LES approach based on high-order compact differencing and filtering schemes (invited). In *16th AIAA Computational Fluid Dynamics Conference*. AIAA 2003-4098.